Advances in Science and Technology Research Journal

Advances in Science and Technology Research Journal 2024, 18(5), 268–276
https://doi.org/10.12913/22998624/190411
ISSN 2299-8624, License CC-BY 4.0

Received: 2024.04.30
Accepted: 2024.07.20
Published: 2024.08.01

Derivation of Material Constants for Experimental SKR-788 Silicone Samples via Simulation Modeling and Laboratory Testing

Vasyl Mykhailiuk[1], Yevstakhiy Kryzhanivskyy[1], Yurii Mosora[1], Ruslan Deineha[1], Damian Dzienniak[2], Szymon Bajda[3], Michał Bembenek[2*]

[1] Department of Oil and Gas Field Machinery and Equipment, Ivano-Frankivsk National Technical University of Oil and Gas, 15 Karpatska st., 76019, Ukraine

[2] Department of Manufacturing Systems, Faculty of Mechanical Engineering and Robotics, AGH University of Krakow, 30-059 Kraków, Poland

[3] Department of Metal Forming and Metallurgical Engineering, Faculty of Metals Engineering and Industrial Computer Science, AGH University of Krakow, 30-059 Kraków, Poland

* Corresponding author's e-mail: bembenek@agh.edu.pl

ABSTRACT

The development of various machines and equipment containing parts or assemblies made of hyperelastic materials (e.g., rubber, silicone) is difficult because of the intricacies involved in the description of their mechanical properties. This is especially seen in calculations using simulation modeling. The behavior of hyperelastic materials is described by utilizing the results of research conducted with specialized equipment. This allows for the most accurate determination of their mechanical properties. Hyperelastic materials are widely used across diverse industries, encompassing mechanical engineering, the chemical and petrochemical sectors, cement production, and beyond. To determine the mechanical characteristics of SKR-788 silicone, batches of test samples were prepared, varying solely in the ratio of the base to the catalyst. Laboratory testing of silicone samples was performed on an Instron 4500 device, and data such as loads, displacements, and deformations were obtained. In order to verify the results of the tests against the results of simulation modeling in Ansys software, a model of the experimental sample was built. The obtained results of uniaxial tensile testing of the experimental sample were taken into account during the description of the material in the Mooney–Rivlin model. The calculation scheme for the test sample during simulation modeling is similar to the one used during its laboratory testing. Applying the load to the test sample during the simulation proceeded incrementally based on time. As a result of the work, the constants of the SKR-788 silicone material for the three-parameter Mooney–Rivlin model were defined (C_{10} = −0.10335 MPa, C_{01} = 0.57534 MPa, and C_{11} = 0.093309 MPa). As a result of simulation modeling of the experimental silicone sample, the values of its displacements and stresses were obtained. Upon comparing the stress values derived from the results of laboratory testing on the Instron 4500 equipment with those obtained from simulation modeling, a discrepancy of up to 7% was identified. For the first time, the characteristics of the SKR-788 silicone material have been established and verified. This will facilitate the design and research of various equipment and machine components made from hyperelastic materials.

Keywords: hyperelastic material, prototype test, silicone, simulation modeling, stress, strain, Mooney–Rivlin model.

INTRODUCTION

The complexity in designing various products made of hyperelastic materials often stems from the intricacies involved in describing their mechanical properties [1]. This is particularly observed in calculations using simulation modeling. In characterizing the behavior of hyperelastic materials, researchers typically rely on data obtained from tests that measure the relationship between stresses and deformations [2]. The mechanical properties of these materials can vary

dependent on factors such as the composition of their components, their proportions, and other related variables. Even though processing parameters can affect the specific tensile strength of the more typical 3D-printable materials, such as PLA or PET-G [3, 4], their behavior is more predictable than that of hyperelastic ones.

Known for their capacity to undergo significant deformations under loading, hyperelastic materials have garnered considerable attention in the past few years, which is confirmed by the amount of recent work done in this area. For example, Zhang et al. delved into the complexities of integrating finite-deformation viscoelastic-hyperelastic materials within a multimaterial design framework [5]. Arbind et al. introduced a comprehensive higher-order shell theory tailored for analyzing the large deformations of shell structures composed of compressible hyperelastic materials [6].

Topology optimization, a critical aspect of structural design, received innovative treatment from Junker et al., who proposed a novel approach grounded in thermodynamic extremal principles specifically designed for hyperelastic structures [7]. Ye et al. grappled with the challenge of tracking crack propagation in nearly incompressible hyperelastic materials, offering enhanced assumed strain methods to aid in energy decomposition [8].

Fernández et al. explored the realm of anisotropic hyperelastic constitutive models for finite deformations, amalgamating material theory with data-driven approaches, particularly focusing on cubic lattice metamaterials [9]. In a similar vein, Zhang et al. devised a multi-material topology optimization framework specifically tailored for hyperelastic materials facing large deformations [10].

Further still, researchers explored specific applications and material modifications. Jamshidian et al. delved into the nonlinear buckling analysis of soft lattice metamaterials composed of hyperelastic materials [11]. Cholleti et al. focused on stress relaxation behavior in barium titanate-silicone elastomer composites, observing a shift toward visco-hyperelastic properties due to the addition of barium titanate particles [12]. Valizadeh et al. explored the tailoring of functionally graded hyperelastic materials through grayscale mask stereolithography 3D printing [13].

Finally, Zhan et al. proposed a new micro–macro transition model tailored specifically for hyperelastic materials, offering insights into bridging different scales of analysis [14]. Collectively, these investigations emphasize the significance of comprehending and optimizing the behavior of hyperelastic materials across diverse loading conditions, with implications for both structural design and material advancement.

Given the ongoing progress in this area, the investigation of the characteristics of hyperelastic materials remains a pertinent focus for international scientists and researchers [15, 16]. Silicone, akin to highly elastic polymer blends, is a good example of a hyperelastic material, exhibiting nonlinear relationships between deformation and stress during loading and unloading.

The most common models for describing the behavior of hyperelastic materials are Neo-Hookean [17, 18], Mooney–Rivlin [19, 20] and Yeoh [21–23] models. They provide a theoretical basis for the analysis of such structures. The selection of an appropriate model during simulation is crucial for effectively addressing engineering challenges, especially when combining simulation modeling with field testing to determine the material's stress–strain relationship [24]. An example of application of the Mooney–Rivlin model is the study by Matli et al. on the failure curve for an interface crack between single crystal silicon and silicone rubber, the results of which highlighted the importance of this model in predicting material behavior accurately [25].

On a more practical note, owing to their characteristics, hyperelastic materials have found widespread application across various industries. For instance, in the development of new product designs such as adjustable Laval nozzles [26], utilizing hyperelastic seals in a universal preventer [27] can expedite the design process, enabling the exploration of numerous potential configurations and experimental outcomes. Moreover, hyperelastic materials, including silicone, can be used in the production of soft structures, such as seals, gaskets, medical implants [28], or structures in soft robotics [29–31]. The unique properties of such materials also make them well-suited for use in belt conveyor systems, where they can help improve performance, reliability, and longevity [32, 33]. Furthermore, layered hyperelastic structures, among which we also find those made of silicone, are utilized in food packaging to provide both a soft, safe interior layer and a stiffer exterior layer [1].

With those points in mind and the potential use cases, the purpose of this work was to verify the results of silicone testing and simulation modeling for further use of the obtained values of

material constants in the design of various products, as there appears to be no record of those constants being derived for this particular type of material in the subject literature. This renders the present work valuable and practically useful while also bringing a novelty from a scientific viewpoint.

MATERIALS AND METHODS

Sample preparation and laboratory tests

In order to ascertain the mechanical properties of SKR-788 silicone [34], batches of test samples were made based on the dimensions outlined in Figure 1. To facilitate the extraction of silicone samples from the mold, a release wax separating paste [35] was applied, specifically designed to ensure easy separation between silicone, polyurethane, and other forming materials. The characteristics of SKR-788 silicone are given in Table 1.

The differences between batches of experimental samples are the ratio of base and catalyst (Table 2). According to the manufacturer's recommendations [34] for SKR-788 silicone, the base/catalyst ratio is 100:2. The silicone samples were tested on an Instron 4500 machine (Instron, Norwood, MA, USA). Figure 2 shows an unloaded test specimen (fixed only).

The test results yielded the following parameters: "Load (N)," "Time (s)," "Extension (mm)," "Stress (MPa)," and "Strain (–)." These results were compiled into a txt format file, which could easily be exported to the Ansys Workbench software for further analysis. The findings from this research can be utilized in the design development of machinery and equipment across various industries [36–38].

Table 2. Designations of test samples and their base/catalyst ratio

No.	Sample ID	Base/catalyst ratio
1	1_1	90:2
2	1_2	
3	1_3	
4	2_1	100:3
5	2_2	
6	2_3	
7	2_4	

Before the test, all samples were surface-cleaned of any remaining uncured resin using ethyl alcohol. Then, the samples were marked to determine the gauge length. Subsequently, each sample was mounted in the grips so that the end of the grip was at the boundary of the gauge length. To prevent the samples from slipping out of the grips during deformation, elastomeric pads with a total thickness equivalent to twice the sample's thickness were used on both sides in the grips.

Simulation modeling

3D model of the test sample and finite element mesh

A 3D model of the experimental sample was built for simulation modeling (Figure 3). The finite element mesh was constructed using the "MultiZone" tool in Ansys with the Mapped

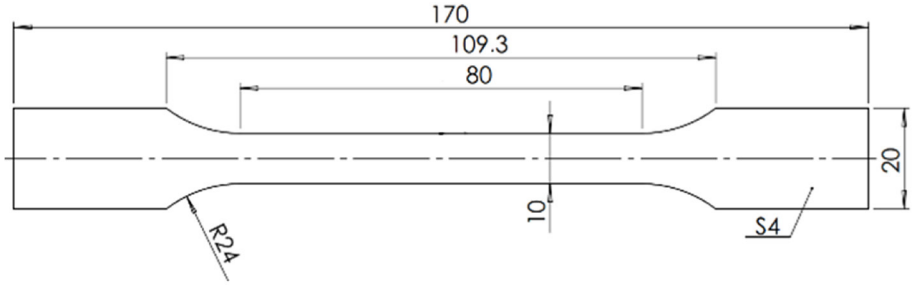

Figure 1. Experimental sample

Table 1. Characteristics of SKR-788 silicone

Characteristic	Average viscosity	Lifetime	Hardness (according to Shore A)	Tensile strength, kN/m	Relative elongation at break, %	Conditional tensile strength, MPa	Ratio of base and catalyst	Linear shrinkage, %	Operating temperature range, °C	Density, g/cm^3, at 25°C
Indicator	19,000 cps at 25 °C	from 30 min at 25 °C	30 ± 3	23	580	3.5	100:2	0.3	−60 + 250	1.1

Figure 2. Instron 4500 testing machine

Mesh Type set to Hexa. The element size was defined as 2 mm. The mesh consisted of 3280 finite elements and 17,165 nodes, where each element had three linear degrees of freedom. Hyperelastic materials like silicone require a fine mesh to capture large deformations and nonlinear stress–strain behavior accurately. A mesh consisting of 3280 elements ensures that critical features and regions of interest are well-resolved. This number, while not strictly defined for this particular type of material and the geometry of the sample, seemed to provide a reasonable compromise between computational cost and the precision of the simulation. Moreover, increasing the number of elements further did not yield any noticeable improvements or differences as far as the obtained results were concerned. The ultimately chosen finite element mesh is shown in Figure 4.

Boundary conditions and settings

During simulation modeling, two types of boundary conditions were applied to the surfaces

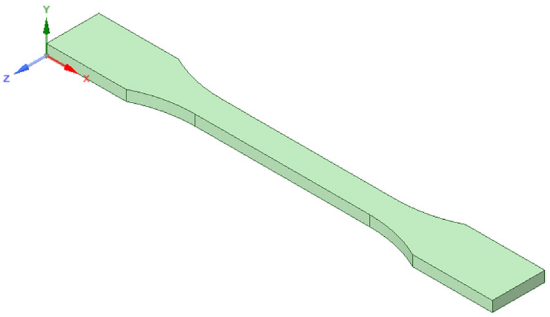

Figure 3. 3D model of the experimental sample

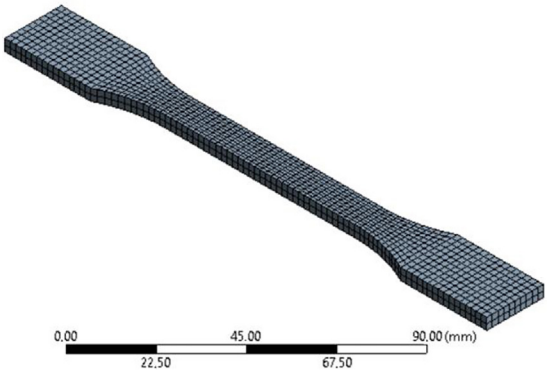

Figure 4. Finite element mesh

of the 3D model of the sample: *Fixed*, where the surfaces were immobilized, and *Displacement*, where the corresponding surfaces were allowed to move according to specified displacements. The calculation scheme is shown in Figure 5.

Displacement was divided into 18 steps depending on time (Table 3). These data were taken from the tensile test of the model, but their number had been reduced for ease of handling.

The calculation scheme for studying the 3D model of the sample is similar to the scheme used when testing it on the Instron 4500 equipment.

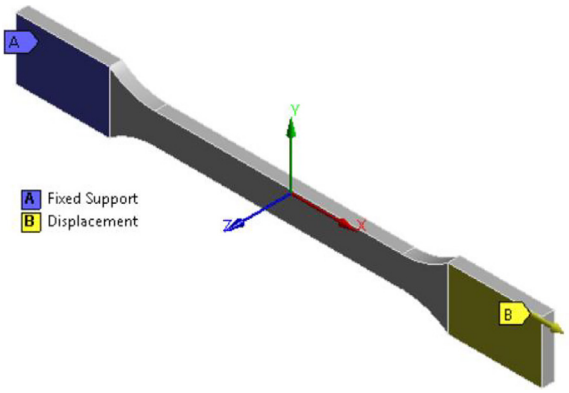

Figure 5. Calculation scheme

Characteristics of the material

During the simulation modeling of the hyperelastic material, the Mooney–Rivlin model [39–41] was employed. Like in other hyperelastic models, elastic strain energy was used to characterize mechanical properties. The Mooney–Rivlin model offers four variants distinguished by the order of the polynomial: two-parameter, three-parameter, five-parameter, and nine-parameter formulations of strain energy. The form of the strain-energy potential for a two-parameter Mooney–Rivlin model is expressed as follows:

$$W = C_{10}(\bar{I}_1 - 3) + C_{01}(\bar{I}_2 - 3) + \frac{1}{D_1}(J-1)^2 \quad (1)$$

where: C_{10}, C_{01}, D_1, – material constants; $\bar{I}_1$ – first invariant of the strain tensor; $\bar{I}_2$ – second invariant of the strain tensor.

The form of the strain-energy potential for a three-parameter Mooney–Rivlin model is:

$$W = C_{10}(\bar{I}_1 - 3) + C_{01}(\bar{I}_2 - 3) + C_{11}(\bar{I}_1 - 3)(\bar{I}_2 - 3) + \frac{1}{D_1}(J-1)^2 \quad (2)$$

The form of the strain-energy potential for a five-parameter Mooney–Rivlin model is:

$$W = C_{10}(\bar{I}_1 - 3) + C_{01}(\bar{I}_2 - 3) + C_{20}(\bar{I}_1 - 3)^2 + C_{11}(\bar{I}_1 - 3)(\bar{I}_2 - 3) + C_{02}(\bar{I}_2 - 3)^2 + \frac{1}{D_1}(J-1)^2 \quad (3)$$

The form of the strain-energy potential for a nine-parameter Mooney–Rivlin model is:

$$W = C_{10}(\bar{I}_1 - 3) + C_{01}(\bar{I}_2 - 3) + C_{20}(\bar{I}_1 - 3)^2 + C_{11}(\bar{I}_1 - 3)(\bar{I}_2 - 3) + C_{02}(\bar{I}_2 - 3)^2 + C_{30}(\bar{I}_1 - 3)^3 + C_{21}(\bar{I}_1 - 3)^2(\bar{I}_2 - 3) + C_{12}(\bar{I}_1 - 3)(\bar{I}_2 - 3)^2 + C_{03}(\bar{I}_2 - 3)^3 + \frac{1}{D_1}(J-1)^2 \quad (4)$$

A higher-order potential can model more complex strain-stress relationships but requires more computational effort and a larger set of experimental data. At the same time, as the nonlinearity increases, the higher-order models may struggle to converge. The three-parameter Mooney–Rivlin model was chosen for the study of the silicone samples.

RESULTS AND DISCUSSION

Figure 6 shows the dependences of stresses on displacements for test samples obtained from the results of testing on the Instron 4500 equipment. Table 3 shows the test results for experimental sample 1_3. As mentioned previously, displacement was divided into 18 steps depending on time, while the load was being increased.

Based on the results of the silicone sample tests, the dependence shown in Figure 7 was constructed using the tools available in the Ansys Workbench software environment, and the material constants of the Mooney–Rivlin three-parameter model were obtained. Table 4 shows the silicon constants for the three-parameter Mooney–Rivlin model.

Simulation results, both for displacements and normal stresses, have been shown in Figures 8 and 9, respectively.

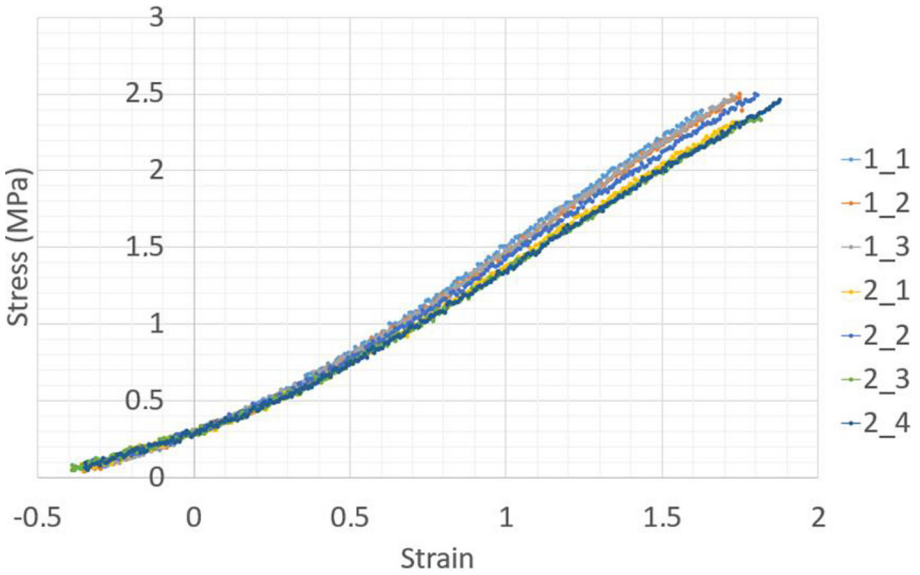

Figure 6. Dependence of stresses on displacements for the experimental silicon sample

Table 3. Test results for experimental sample 1_3

No.	Load (N)	Time (s)	Extension (mm)	Stress (MPa)	Strain (–)
1	12.2	3.08	0.2	0.29	0.003
2	15.5	4.00	7.8	0.38	0.098
3	19.1	5.02	16.4	0.47	0.205
4	23.5	6.05	24.9	0.57	0.311
5	28.0	7.02	33.1	0.68	0.413
6	32.9	8.02	41.4	0.80	0.517
7	38.4	9.02	49.7	0.94	0.622
8	44.3	10.02	58.0	1.08	0.726
9	49.7	11.02	66.4	1.21	0.830
10	56.1	12.02	74.7	1.37	0.934
11	62.2	13.02	83.0	1.52	1.038
12	68.3	14.02	91.4	1.67	1.143
13	75.4	15.08	100.2	1.84	1.253
14	81.4	16.02	108.0	1.99	1.350
15	86.9	17.02	116.4	2.12	1.455
16	91.6	18.02	124.7	2.24	1.559
17	98.7	19.00	132.9	2.41	1.661
18	101.2	19.66	138.4	2.47	1.730

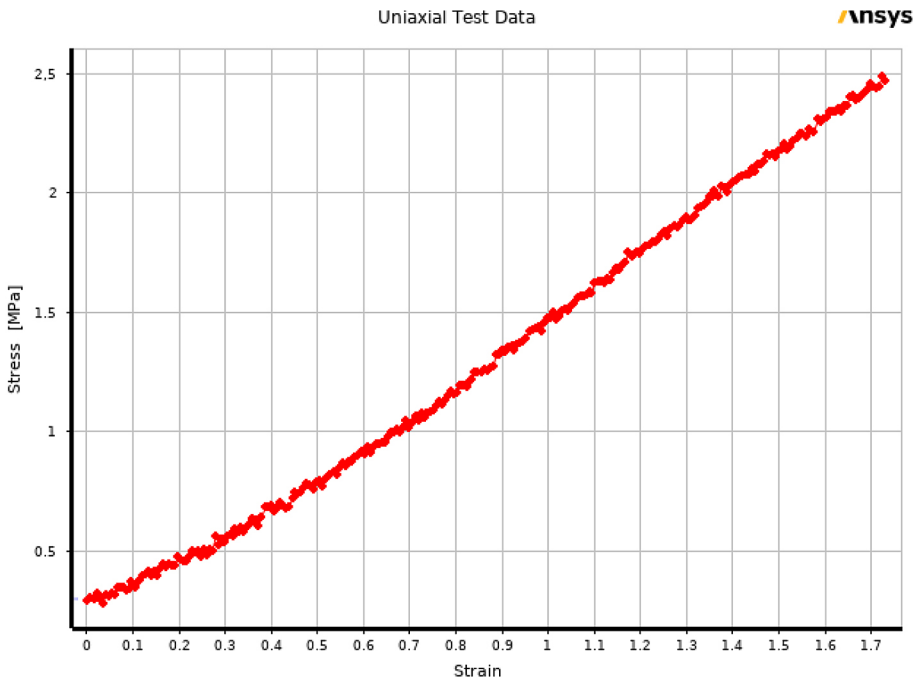

Figure 7. Dependence of stresses on the deformation of the experimental silicone sample in the Ansys Workbench software environment

As Figure 8 suggests, the maximum amount of displacement in the test sample is 138.4 mm, and as per Figure 9, the maximum amount of normal stress is 2.6496 MPa. A discrepancy of up to 7% was observed when comparing the stress values obtained from testing on the Instron 4500

Table 4. Silicon constants of the three-parameter Mooney–Rivlin model

Parameter	Value	Unit
Material constant C_{10}	−0.10335	MPa
Material constant C_{01}	0.57534	
Material constant C_{11}	0.093309	

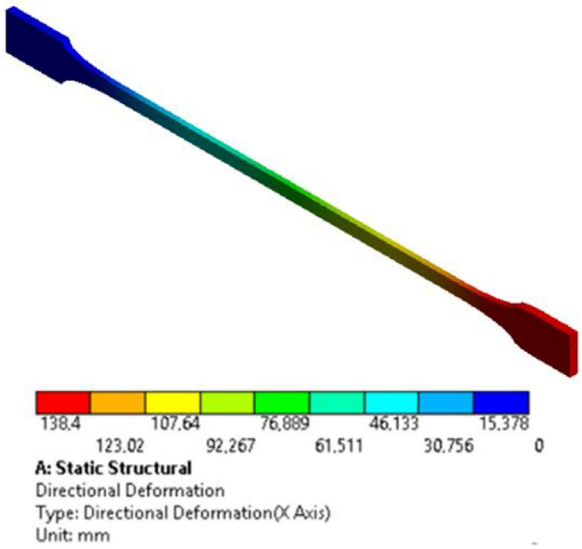

Figure 8. Directional deformation (X Axis)

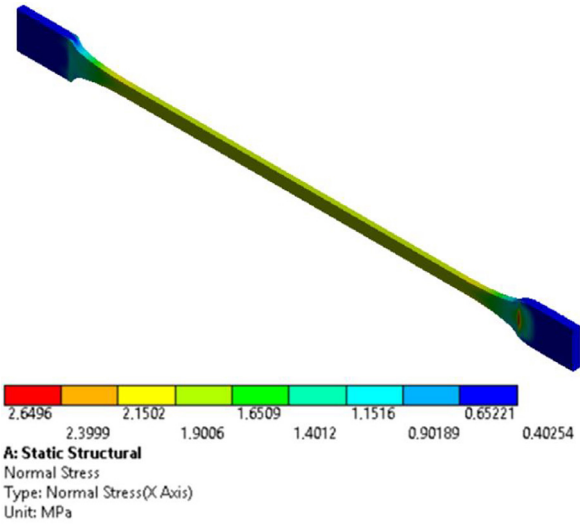

Figure 9. Normal stresses (X Axis)

equipment with those obtained through simulation modeling in the Ansys Workbench software environment. The effect of the ratio of base and catalyst (90:2 and 100:3) for SKR-788 silicone does not significantly affect its mechanical properties. However, this ratio affects the curing time of the silicone.

CONCLUSIONS

Hyperelastic materials, like the SKR-788 silicone analyzed in this work, require the use of sophisticated material models, such as the Mooney–Rivlin model, to describe their nonlinear behavior accurately. When performing laboratory testing, it is essential to ensure that the samples are prepared with uniform dimensions and free from defects or imperfections that could affect the test results. It is also important to select an appropriate gripping method (e.g., pneumatic, hydraulic, or mechanical grips) that minimizes stress concentrations and ensures uniform loading of the specimen.

The Instron 4500 universal testing machine was used to perform the testing of the SKR-788 silicone samples, which in turn made it possible to derive the three material constants for this type of material according to the three-parameter Mooney–Rivlin model: $C_{10} = -0.10335$ MPa, $C_{01} = 0.57534$ MPa, and $C_{11} = 0.093309$ MPa. The experimental results of the uniaxial strain tests were also verified against the results of simulation modeling using Ansys Workbench without showing much discrepancy. For the first time, the constants of SKR-788 silicone have been determined, and in the future they may be used in the process of developing various products that rely on this material.

Acknowledgments

The present article originated as part of the research internships "Using advanced FEM modeling to simulate mechanical engineering processes" by Vasyl Mykhailiuk and "Solving optimization problems in mechanical engineering using advanced FEM modeling" by Ruslan Deineha at the AGH University of Krakow, Faculty of Mechanical Engineering and Robotics, Department of Manufacturing Systems.

REFERENCES

1. Khaniki H.B., Ghayesh M.H., Chin R., Amabili M. A review on the nonlinear dynamics of hyperelastic structures. Nonlinear Dynamics 2022; 110(2): 963–994.
2. Falope F.O., Pelliciari M., Lanzoni L., Tarantino A.M. Snap-through and Eulerian buckling of the bi-stable von Mises truss in nonlinear elasticity: A theoretical, numerical and experimental investigation. International Journal of Non-Linear Mechanics 2021; 134: 103739.
3. Bembenek M., Kowalski Ł., Pawlik J., Bajda S. Research on the influence of the load direction and the cross-section shape on the Young's modulus of elements produced by the fused deposition modeling method. Journal of Materials Engineering and Performance 31(10): 7906–7912.

4. Bembenek M., Kowalski Ł., Kosoń-Schab A. Research on the influence of processing parameters on the specific tensile strength of FDM additive manufactured PET-G and PLA materials. Polymers 2022; 14(12): 2446.
5. Zhang G., Khandelwal K. Design of dissipative multimaterial viscoelastic-hyperelastic systems at finite strains via topology optimization. International Journal for Numerical Methods in Engineering 2019; 119(11): 1037–1068.
6. Arbind A., Reddy J.N., R. Srinivasa A. A general higher-order shell theory for compressible isotropic hyperelastic materials using orthonormal moving frame. International Journal for Numerical Methods in Engineering 2021; 122(1): 235–269.
7. Junker P., Balzani D. A new variational approach for the thermodynamic topology optimization of hyperelastic structures. Computational Mechanics 2021; 67(2): 455–480.
8. Ye J.Y., Zhang L.W., Reddy J.N. Large strained fracture of nearly incompressible hyperelastic materials: Enhanced assumed strain methods and energy decomposition. Journal of the Mechanics and Physics of Solids 139: 103939.
9. Fernández M., Jamshidian M., Böhlke T., Kersting K., Weeger O. Anisotropic hyperelastic constitutive models for finite deformations combining material theory and data-driven approaches with application to cubic lattice metamaterials. Computational Mechanics 2021; 67(2): 653–677.
10. Zhang X.S., Chi H., Paulino G.H. Adaptive multimaterial topology optimization with hyperelastic materials under large deformations: A virtual element approach. Computer Methods in Applied Mechanics and Engineering 2020; 370: 112976.
11. Jamshidian M., Boddeti N., Rosen D., Weeger O. Multiscale modelling of soft lattice metamaterials: Micromechanical nonlinear buckling analysis, experimental verification, and macroscale constitutive behaviour. International Journal of Mechanical Sciences 2020; 188: 105956.
12. Cholleti E.R., Stringer J., Kelly P., Bowen C., Aw K. The effect of barium titanate ceramic loading on the stress relaxation behavior of barium titanate-silicone elastomer composites. Polymer Engineering & Science 2020; 60(12): 3086–3094.
13. Valizadeh I., Al Aboud A., Dörsam E., Weeger O. Tailoring of functionally graded hyperelastic materials via grayscale mask stereolithography 3D printing. Additive Manufacturing 2021; 47: 102108.
14. Zhan L., Wang S., Qu S., Steinmann P., Xiao R. A new micro–macro transition for hyperelastic materials. Journal of the Mechanics and Physics of Solids 2023; 171: 105156.
15. Wang H., Cao S., Luo X., Zhang Z., Wu Q. Experimental study on the effect of rubber isolator on the vibration of piston pump. In: Proceedings of the 6th International Conference on Control, Mechatronics and Automation [Internet] New York, NY, USA: Association for Computing Machinery; 2018 [cited 2024 Apr 25]. 111–115. (ICCMA 2018). Available from: https://dl.acm.org/doi/10.1145/3284516.3284519
16. Dorokhov M.A., Kostryba I.V. Computer modeling of stress-strain state seals well packer. Oil and Gas Engineering 2016; 1: 103–110.
17. Mei Y., Stover B., Afsar Kazerooni N., Srinivasa A., Hajhashemkhani M., Hematiyan M.R., Goenezen S. A comparative study of two constitutive models within an inverse approach to determine the spatial stiffness distribution in soft materials. International Journal of Mechanical Sciences 2018; 140: 446–454.
18. Chung I., Im S., Cho M. A neural network constitutive model for hyperelasticity based on molecular dynamics simulations. International Journal for Numerical Methods in Engineering 2020; 122.
19. López-Campos J., Segade A., Fernández J., Casarejos E., Vilán J. Behavior characterization of visco-hyperelastic models for rubber-like materials using genetic algorithms. Applied Mathematical Modelling 2019; 66: 241–255.
20. Shariyat M., Khosravi M., Yazdani Ariatapeh M., Najafipour M. Nonlinear stress and deformation analysis of pressurized thick-walled hyperelastic cylinders with experimental verifications and material identifications. International Journal of Pressure Vessels and Piping 2020; 188: 104211.
21. Gajewski M., Szczerba R., Jemioło S. Modelling of elastomeric bearings with application of Yeoh hyperelastic material model. Procedia Engineering 2015; 111: 220–227.
22. Korba A.G., Barkey M.E. New model for hyperelastic materials behavior with an application on natural rubber. In Los Angeles, California, USA: American Society of Mechanical Engineers Digital Collection; 2017 [cited 2024 Apr 24]. Available from: https://dx.doi.org/10.1115/MSEC2017-2792
23. Bhat S.K., Power-Yeoh A.K. A yeoh-type hyperelastic model with invariant I2 for rubber-like materials. Engineering Proceedings 2023; 59(1): 104.
24. Zhao Z., Mu X., Du F. Modeling and verification of a new hyperelastic model for rubber-like materials. Mathematical Problems in Engineering 2019; 2019(1): 2832059.
25. Matli S.R., Rubin E., Banks-Sills L. Mixed mode failure curve for an interface crack between single crystal silicon and silicone rubber. Theoretical and Applied Fracture Mechanics 2022; 122: 103640.
26. Mykhailiuk V.V., Liakh M.M., Protsiuk V.R., Deineha R.O., Vytrykhovskyi Ye.A., Stetsiuk R.B. Development of the adjustable Laval nozzle design. Oil

and Gas Power Engineering 2022; 2(38): 85–92.

27. Mykhailiuk V.V., Chudyk I.I., Mosora Y. On the possibility of using simulation modeling for research and design of universal preventer seals. Scientific Bulletin of Ivano-Frankivsk National Technical University of Oil and Gas 2021; 1(50): 53–61.
28. Schendel M.J., Popelar C.F., Martin D. Numerical methods for design and evaluation of prosthetic heart valves. In: Iaizzo PA, Iles TL, Griselli M, St. Louis JD, editors. Heart Valves: From Design to Clinical Implantation [Internet] Cham: Springer International Publishing; 2023 [cited 2024 Apr 26]. 487–508. Available from: https://doi.org/10.1007/978-3-031-25541-0_17
29. Chen L., Yang C., Wang H., Branson D.T., Dai J.S., Kang R. Design and modeling of a soft robotic surface with hyperelastic material. Mechanism and Machine Theory 2018; 130: 109–122.
30. Vignali E., Gasparotti E., Capellini K., Fanni B.M., Landini L., Positano V., Celi S. Modeling biomechanical interaction between soft tissue and soft robotic instruments: importance of constitutive anisotropic hyperelastic formulations. The International Journal of Robotics Research 2021; 40(1): 224–235.
31. Yap H.K., Lim J.H., Nasrallah F., Yeow C.H. Design and preliminary feasibility study of a soft robotic glove for hand function assistance in stroke survivors. Frontiers in Neuroscience [Internet] 2017; 11. Available from: https://www.frontiersin.org/journals/neuroscience/articles/10.3389/fnins.2017.00547/full
32. Bertini L., Carmignani L., Frendo F. Analytical model for the power losses in rubber V-belt continuously variable transmission (CVT). Mechanism and Machine Theory 2014; 78: 289–306.
33. Kolosov D., Dolgov O., Bilous O., Kolosov A. The stress-strain state of the belt in the operating changes of the burdening conveyor parameters. New Developments in Mining Engineering 2015: Theoretical and Practical Solutions of Mineral Resources Mining 2015; 585: 590.
34. SKR-788—Silicone for molds [Internet]. 2024 [cited 2024 Apr 25]. Available from: https://silikoni.com.ua/skr-788-silikon-dlya-form/ (in Ukrainian)
35. Wax separator for molds (paste)—40 grams [Internet]. [cited 2024 Apr 25]. Available from: https://silikoni.com.ua/release-wax-voskova-rozdilova-pasta-40-hram/ (in Ukrainian)
36. Mykhailiuk V., Zasadzień M., Liakh M., Deineha R., Mosora Y., Faflei O. Analysis of the possibility of modeling gas separators using computational fluid dynamics. Management Systems in Production Engineering 2024; 32: 80–86.
37. Grydzhuk J., Chudyk I., Slabyi O., Mosora Y., Kovbaniuk M., Krynke M. Mathematical modeling of the stress-strain state of the annular preventer seal using the theory of reinforced shells. Production Engineering Archives 2022; 28(4): 375–380.
38. Vytyaz O., Ivasiv O., Rachkevych R., Deynega R. Research on the influence of the repair sleeves on the strength and the stress-strain state of the pipeline section. Nafta-Gaz 2022; 78(10): 733–739. (in Polish)
39. Mooney M. A theory of large elastic deformation. Journal of Applied Physics 1940; 11(9): 582–592.
40. Rivlin R.S. Large elastic deformations of isotropic materials. VI. Further results in the theory of torsion, shear and flexure. Philosophical Transactions of the Royal Society of London Series A Mathematical and Physical Sciences 1949; 242: 173–195.
41. WELSIM. Mooney-Rivlin hyperelastic model for nonlinear finite element analysis [Internet]. Medium. 2020 [cited 2024 Apr 26]. Available from: https://getwelsim.medium.com/mooney-rivlin-hyperelastic-model-for-nonlinear-finite-element-analysis-b0a9a0459e98